DIOGENESS

Soft X-ray Spectrometer-photometer for Studies of Flare Energy Balance

J. Sylwester[1]), F. Fárník[2])

1) *Space Research Centre of the Polish Academy of Sciences, Wroclaw, Poland*
2) *Astronomical Institute, Czechoslovak Academy of Sciences, 251 65 Ondřejov, Czechoslovakia*

ДИОГЕНЕС — СПЕКТРОМЕТР-ФОТОМЕТР МЯГКИХ Х-ЛУЧЕЙ
ДЛЯ УЧЕНИЯ БАЛАНСА ЭНЕРГИИ ВСПЫШЕК

В равоте описаны научные цели и технические характеристики прибора ДИОГЕНЕС (это название возникло сокращением английского описания цели измерения: диагностика источников и потребителей энергии в солнечных вспышках). Этот прибор конструируется для автоматической солнечной обсерватории КОРОНАС-И, которая должна быть выведена на орбиту в начале 90-ых годов в рамках сотрудничества Интеркосмос.

We describe the scientific objectives and the technical characteristics of the DIOGENESS (Diagnostic of Energy Sources and Sinks in flares) instrument which is under development for the CORONAS-I solar observatory to be launched in the early 1990's as part of the INTERCOSMOS programme.

1. Introduction

In the late 1980's INTERCOSMOS announced tentative project of launching two satellites, CORONAS I and CORONAS F, designed to study the solar atmosphere during and after the maximum of solar activity cycle 22. In response to this, the Space Research Centre of the Polish Academy of Sciences (SRC) and the Astronomical Institute of the Czechoslovak Academy of Sciences (AI CsAS) developed jointly a proposal of the DIOGENESS instrument devoted to the studies of the global energy balance in flares (Tab. I). The instrument consists of three physi-cally separate units: a Bragg high-resolution spectrometer (BS), a soft-hard X-ray photometer (BF), and a microcomputer (PRAM) for steering and control, as well as data processing for the two units mentioned above and for some other instruments aboard CORONAS. The BS and BF units are planned as part of the instrument payload (open space), while PRAM is to be located in the pressurized, thermally controlled section of the satellite. This paper describes the scientific aspects of the DIOGENESS instrument and contains general information on the construction of the spectrometer block which is under development in the SRC, as well as the photometer block and the

Table I

General Characteristics of DIOGENESS

Block	BS	BE	PRAM
Size (mm)	160 × 330 × 334	153 × 230 × 254	120 × 150 × 200
Weight (kg)	6·1	6·0	2·1
Power consumption (W) (max)	15	6	3
(mean)	8	6	2
Max transmiss.	1200	200	1200
rate (bit/s)	to/from PRAM	to PRAM	to Telemetry
Location	Open Space		Press. Container

PRAM, which are being developed at the AI CsAS under a design similar to that adopted for the broad-band X-ray photometers for the PROGNOZ and INTERBOL missions (see Fárník et al. 1984). DIOGENESS shares a part (12 Mbits) of the SSNI telemetry memory (SSNI is one of the two main telemetry systems with receiving ground stations in the USSR) to store the results of measurements between the telemetry transmissions. A special two-way telemetry radio-link under development at the AI CsAS, allows for transmission of the content of the PRAM data memory to the telemetry stations in Czechoslovakia and/or Poland during radio visibility (at least twice a day) and for two-way communication with the PRAM computer which enables us to receive a part of the measured data in Czechoslovakia or Poland without any delay. The two-way communication makes it possible to relay commands to the PRAM and, if necessary, to update on-board software. The PRAM is linked with the BF by a parallel communication line and with the BS via a sequential communication line served by the BS inner microprocessor (type Z 80).

2. Scientific Objectives

The ultimate goal of the DIOGENESS instrument is to provide measurements which will allow the balance of the solar flare energy, contained in its main thermal reservoir, to be studied. Studies of the energy balance are important for a better understanding of the flare mechanisms and processes leading to energy deposition, transport and redistribution between its various forms. It has been extensively discussed in the literature that important components of the flare plasma energy are: the thermal energy E_{th}, the energy deposited in the form of heat at the volumetric rate E_H (ergs cm^{-3} s^{-1}), the energy radiated by the plasma at the rate E_R, the energy conducted away at the rate E_c, the energy which flows in or out at the rate E_{conv} (into/out of the region, with the moving plasma), the energy contained in the turbulent motions of the plasma E_{Turb}, and the energy contained in the accelerated particles E_{Acc}. As follows from Chapter 5 of "Energetic Phenomena on the Sun", (1986), the energy terms related to the increase of the potential energy of the evaporated plasma and the kinetic energy of the inflowing plasma may be regarded as insignificant in comparison with the other energies. B. Sylwester at al. (1987, 1988) have used the following relations for calculating the individual energy terms based on the observable physical characteristics of the flaring plasma: *The thermal energy*

$$E_{th} = 3kT_{av}(\varepsilon V)^{1/2} \,, \tag{1}$$

where T_{av} is the average plasma temperature in the plasma region with temperatures above T_{min}, ε is the emission measure of this plasma and V is the volume occupied by this plasma: k is the Boltzman constant. The minimum temperature T_{min} represents the equivalent minimum temperature of the source plasma which can be determined for each of the studied lines or broad-band channels, see B. Sylwester et al. (1989). In the case of DIOGENESS T_{min} should be between 4 MK and 10 MK.

The volumetric rate of heating

$$E_H = \frac{\varkappa_0 T_{max}^{7/2}}{L^2} \,, \tag{2}$$

where $\varkappa_0$ is the coefficient in the expression for classical thermal conductivity, T_{max} is the actual maximum temperature of the thermal plasma in the flaring volume and L is the characteristic semilength of the flaring structure (loop). *The radiative losses rate*

$$E_R = \varepsilon P_r(T_{av}) \,, \tag{3}$$

where P_r is the radiative loss power which may be estimated for known T_{min} as shown by B. Sylwester et al. (1987). *The conductive losses rate*

$$E_c = 2\varkappa_0 A(T_{min})^{5/2} \frac{dT}{dl} \tag{4}$$

can be expressed in terms of the observables as:

$$E_c = 2\varkappa_0 f A(T_{max})^{7/2} L^{-1} \,, \tag{5}$$

where A is the cross-section of the flaring flux tube and f represents an average scaling factor related to the approximate treatment of the local temperature gradient (see the above reference for details). *The convective rate*

$$E_{conv} = \alpha E_c \,, \tag{6}$$

where α is the fraction of the flux conducted from the higher temperature region which returns back convectively and is close to 1 (see the above reference). For some flares the effective geometrical parameters may be estimated by integrating the energy balance equation in time based on the evolution of the three parameters namely T_{max}, T_{av} and ε. The procedure leading to the estimation of A and L, and consequently to the solution of the energy balance equation has been described by B. Sylwester et al. (1986, 1988) and constitutes the base for the analysis of the parameters derived from the DIOGENESS measurements.

The analysis of emission line profiles in the soft X-ray spectrum of flares provides information on the

magnitude of directed and turbulent motions present in the thermal plasma. The measured intrinsic FWHM of the line may be expressed in terms of the v_{rms}, which is the average velocity of the turbulent motion:

$$\text{FWHM} = 2 \left(\ln 2\right)^{1/2} \frac{\lambda}{c} \left(\frac{2kT_{ion}}{M} + v_{rms}^2\right)^{1/2}, \qquad (7)$$

where T_{ion} is the characteristic temperature of kinetic motions of ions producing the line, M is the atomic mass of the corresponding element. It is often assumed that $T_{ion} = T$. This assumption may be verified by DIOGENESS measurements of line widths for elements of various atomic masses. The spectra of initial flare phases observed by the Solar Maximum Mission Bent Crystal Spectrometer and the Solflex instrument aboard the P-78 satellite indicate that for most flares observed on the solar disc, a small blue-shifted component of strong lines is present. The characteristic velocity of the plasma responsible for the blue-shifted emission may vary between 150 to 300 km/s and is commonly related to the average velocity of the material being evaporated from the dense transition region. The kinetic energy carried by the in-flowing plasma in a column of length 1 may be estimated as:

$$E_{Kin} = \tfrac{1}{2} A v_{ev}^2 \varrho l . \qquad (8)$$

Therefore, the measurements of the blue-shifts may lead to the estimation of E_{Kin}. The incident high-energy X-ray spectrum may usually be approximated by a power law:

$$I_x(E) = \alpha' E^{-\gamma} \quad \text{photons cm}^{-2}\,\text{s}^{-1}\,\text{keV}^{-1}, \qquad (9)$$

where $I_x(E)$ is the differential flux of photons with energy E in keV, and α' and γ are parameters determined from least-squares fits to the spectral data. The corresponding spectrum of non-thermal electrons that results in the observed photon spectrum is also a power law, of the form

$$I_\Theta(E) = \beta E^{-\delta} \quad \text{electrons s}^{-1}\,\text{keV}^{-1}, \qquad (10)$$

where $I_\Theta(E)$ is the differential flux of electrons with energy E that enter the thick target. The parameters β and δ are related to α' and γ by the following equations:

$$\beta = 3 \times 10^{33} \alpha' \gamma (\gamma - 1)^2 \, b(\gamma - \tfrac{1}{2}, \tfrac{1}{2}),$$
$$\delta = \gamma + 1, \qquad (11)$$

where b is the beta function. The total energy of electrons that enter a thick target during a flare is

Table II

The list of important lines to be measured by DIOGENESS.

No[+]	λ [Å]	Ion & Transition	Key
1	2·940	Fe XXV $(1s^2 - 1s\,5p\,^1P_1)$	2nd order
2	2·972	Cu XXVIII	2nd order
3	2·987	Ar XVIII $(1s\,^2S_{1/2} - 4p\,^2P_{1/2,3/2})$	
4	3·000	Fe XXV $(1s^2\,^1S - 1s\,4p\,^1P)$	2nd order
5	3·0085	K XVIII $(1s^2\,^1S_0 - 1s\,3p\,^1P_1)$	
6*	3·0185	Ca XX $(1s\,^2S_{1/2}\,2p\,^2P_{3/2})$	Ly$_{\alpha 1}$
7*	3·0239	Ca XX $(1s\,^2S_{1/2}\,2p\,^2P_{1/2})$	Ly$_{\alpha 2}$
8	3·0476	Ca XIX $(1s\,2p\,^1P_1 - 2p^2\,^1D_2)$	J
9	3·100	Ni XXVIII $(1s\,^2S - 2p\,^2P)$	2nd order
10	3·146	Fe XXV $(1s^2\,^1S_0 - 1s\,3p\,^1P_1)$	2nd order
11	3·151	Ar XVIII $(1s\,^2S_{1/2} - 3p\,^2P_{1/2,3/2})$	
12*	3·1781	Ca XIX $(1s^2\,^1S_0 - 1s\,2p\,^1P_1)$	w
13	3·183	Ni XXVII $(1s^2\,^1S_0 - 1s\,2p\,^1P_1)$	2nd order
14	3·1912	Ca XIX $(1s^2\,^1S_0 - 1s\,2p\,^3P_2)$	x
15	3·1945	Ca XIX $(1s^2\,^1S_0 - 1s\,2p\,^3P_1)$	y
16	3·1996	Ar XVII $(1s^2\,^1S_0 - 1s\,4p\,^1P_1)^{++}$	
17	3·202	Ni XXVI $(1s^2\,2p\,^2P_{3/2} - 1s\,2p^2\,^2D_{5/2})$ 2nd order	
18	3·2024	Ca XVIII $(2s\,^2 2s\,^1S_{1/2} - 1s\,2p\,^3P\,1s\,^2P_{3/2})$	q
19	3·2082	Ca XVIII $(1s^2\,2p\,^2P_{1/2} - 1s\,2p^2\,^2D_{3/2})$	k
20	3·2130	Ca XVIII $(1s^2\,2p\,^2P_{3/2} - 1s\,2p^2\,^2D_{5/2})$	j
21	3·2130	Ca XIX $(1s^2\,^1S_0 - 1s\,2s\,^3S_1)$	z
22	3·367	Ar XVII $(1s^2\,^1S_0 - 1s\,3p\,^1P_1)$	

[+] Corresponds to line keys in Fig. 1.

[++] The higher terms of the series up to the ionization threshold located at 3·0086 Å are also seen in the spectrum.

obtained from:

$$E_{Acc} = \int \beta E_0^{-\delta+2}(\delta - 2)^{-1} \, dt . \qquad (12)$$

In this expression, the lower energy cut-off, E_0, must be imposed on the spectrum to ensure that the energy E_{Acc} remains finite. It is very difficult to determine the correct value of E_0 from the observations, but it is usually taken as between 10 and 25 keV. The analysis of DIOGENESS hard X-ray spectra recorded by the photometer may help to define the effective E_0 value based on energy balance considerations. From the discussion and Equations (1) to (12) one can see that the combined analysis of the soft and hard X-ray spectra may lead to the solution of the energy balance equations for the flares, all of whose prerequisite parameters are known. The line intensity and continuum level measurements may be used to analyse the plasma composition. It seems possible that flare abundances may be determined for the following elements: Ca, Ar, K, and possibly Fe, Ni and Cu, if very big flares are observed.

The special construction of the spectrometer allows even small motions of the plasma to be detected, which may help in studying the early phases of transients, possibly related to the eruption of the flare loop system.

3. Estimation of the Characteristic Parameters

In this section we discuss the methods which will be used to estimate the value of the individual characteristic parameters based on the measured line and broad-band fluxes. The portion of the observed solar spectrum, which will be measured by BS, is shown in Fig. 1.

Average Temperature

We are going to estimate T_{av} using the following three ratios:

— the k to w line intensity ratio as determined from the high resolution spectra of the Ca XVIII to Ca XIX ions in the $3 \cdot 16 - 3 \cdot 23$ Å range (line identification is given in Tab. II);

— the Ca XX Ly α to Ca XIX w line intensity ratio;

— the ratio of fluxes measured in bands $2 - 4$ keV and $4 - 8$ keV.

The reference temperature scale will be based on temperatures obtained from the k to w line ratio. The value of the Ly to w ratio may be used to study the ionization state of the plasma. The broad band ratio will be extremely useful in estimating T_{av} in early phases of flare evolution when the spectra are weak (below the sensitivity threshold of the spectrometer). The broad band ratio temperature scale should be calibrated using the k to w temperatures during the later phases of flare evolution (close to flare maximum). The expected time resolution of the broad-band measurements is $0 \cdot 1$ s, while for the spectral measurements it is 10 to 60 s depending on the flare intensity.
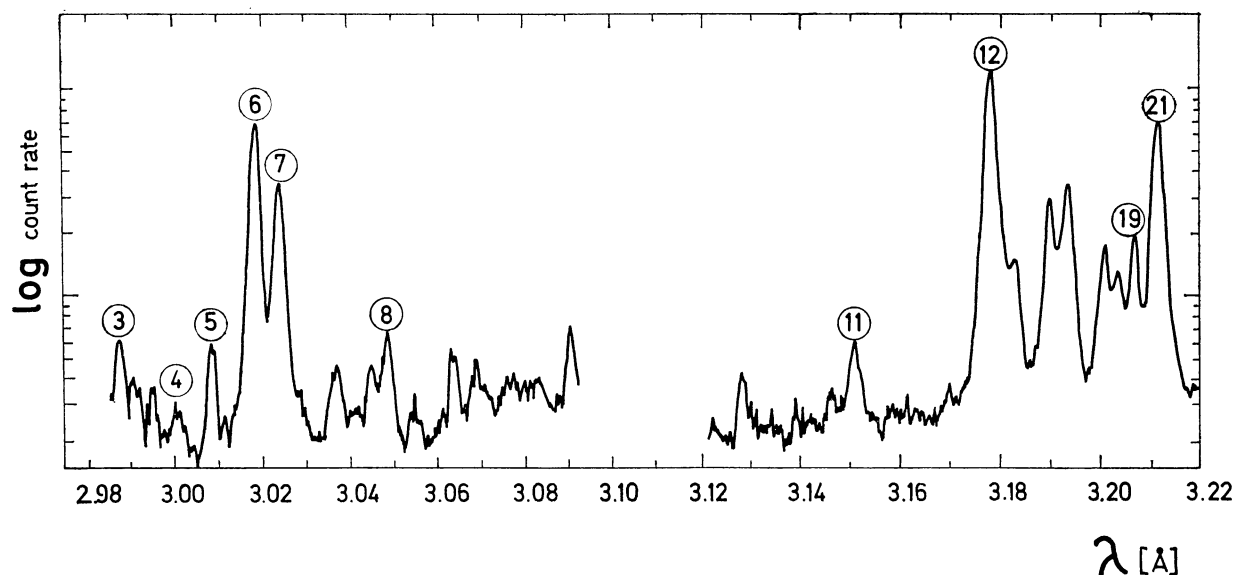

Fig. 1. A sample of the flare spectrum which will be observed by BS. The numbers above the stronger lines correspond to the numbers in Tab. II. The figure has been compiled using the measurements made aboard the NRL P-78 satellite (see Feldman et al. 1980).

Emission Measure

The emission measure (ε) estimations will be based on the value of the absolute fluxes measured in the individual strong spectral lines and on the fluxes measured in low energy broad-band channels. For the ε determination it is necessary to know the average temperature T_{av} (see previous section). It should be noted that the derived emission measure values depend on the absolute calibration of the spectrometer and/or photometer. Therefore substantial efforts are planned to perform a detailed laboratory calibration of all important instrument characteristics (see Chapter 6).

Maximum Temperature

The maximum temperature of the thermal plasma component T_{max} will be estimated using the satellite-to-resonance line intensity ratio in the Ca hydrogen-like ion (J-to-Ly ratio) in the range $3 \cdot 00 - 3 \cdot 05$ Å. High time resolution values will be obtained from the broad-band ratio X2/X3 (see Tab. III).

Table III

Energy bands of the photometer block

Band No	Energy range [kev]	Count rate limits [cts/s]	Detector Type
X1	2— 4	$1-3 \times 10^4$	PC1 + PC2
X2	4— 8	$1-3 \times 10^4$	
X3	10— 20	$1-3 \times 10^4$	SCD
X4	20— 40	$1-1 \times 10^4$	
X5	40— 80	$1-1 \times 10^4$	
X6	80—160	$1-1 \times 10^4$	

Power Law Fitting

By fitting the power law to the observed high-energy X-ray spectra measured by the photometer (channels X3—X6), it will be possible to derive the appropriate parameters (α' and γ) which allow the energy carried by the non-thermal electrons to be estimated. The broad band X-ray spectra will be measured in the bands given in Tab. III.

Line Widths and Blue-Shifts

We are going to estimate the line widths in the process of fitting the synthetic theoretical spectrum to the measured profile, based on the known instrument response function (for details see Fludra et al. 1989). The expected time resolution of the line profile

measurements may be as high as 10 s for stronger flares close to maximum. We will try to measure a profile of a single chosen strong spectral line (see asterisks in Tab. II) as frequently as the count statistics allows.

Abundance Determinations

The appropriate spectra will be recorded mostly in the decay phase of flares, when the characteristic time of variation of the physical conditions in the source is longer than the time to record the individual spectrum. The spectra will be recorded in a relatively wide wavelength interval containing lines from different elements (see Tab. II). In these later phases of flare evolution, when the count rates are high, precise measurements of Doppler line shifts will be especially accurate. Effects of the orbital motion of the Coronas satellite should be pronounced.

4. Design of the Instrument

The Photometer Block

This block contains three types of detectors: two proportional counters (PC) for the soft X-ray region, one scintillation detector (SCD) for the hard X-ray region and three semicondutor detectors for detecting charged particles. The proportional counters are filled with an Ar + 10% CO_2 mixture at 350 Torr and their beryllium windows, 100 μm thick, have areas of 0·1 and 0·01 cm². During low activity the signal from the counter with the larger window is recorded and fed into the telemetry system and during larger flares the second (small-window) counter is recorded. If one of these two counters fails, only the second one is used constantly. Both proportional counters are double-body double-window type with the Fe 55 source on the second window. It enables constant in-flight calibration. The scintillation detector consists of a NaI(TI) crystal (8 mm thickness, 50 mm diameter) and a TESLA-VUVET photomultiplier. The background level in the detector is passively lowered by using a special multilayer heavy shielding of NaI crystal. A small mechanical arm with the Am 241 radioactive source can be moved out of the shielding to calibrate the scintillation channel. Six energy bands are derived from both types of detectors using an amplitude analysis, see Tab. III. All functions of the photometer are controlled by the on-board computer PRAM. In particular, after switching-on, the performance of the detectors and electronics is checked and the detectors are

calibrated using built-in radioactive sources. During the in-orbit operation, the computer selects only the data which contain useful information, reformats them and feeds them to the telemetry with an assigned time mark. The time resolution of the measurements may be changed according to the program, depending on the actual level of the count rate. The detector's high voltage supply is switched off during passages through the radiation belts. In the harder channels (X3 − X6) the time resolution may be decreased down to 0·1 s whereas in the soft channels down to 1 s. Three semiconductor detectors (two redundant) are used mainly to flag the radiation belt passage, but may also be used for uncalibrated measurements of the energetic solar particle fluxes following big flares.

The Spectrometer Block

The general layout of the spectrometer is shown in Fig. 2. It consists of four identical quartz (1011) crystals (first order 2d = 6·6859 Å) organized in two
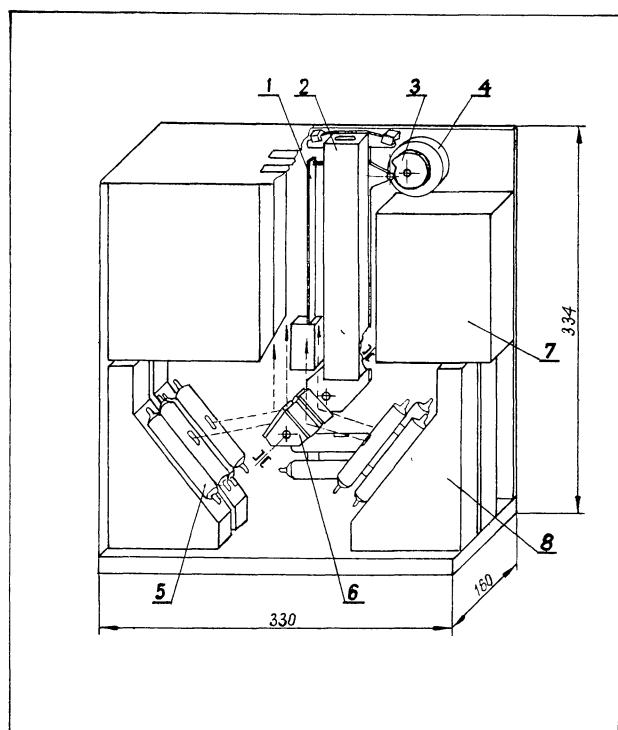

Fig. 2. Isometric drawing showing the Photometer Block of DIOGENESS (dimensions are in millimeters). The numbers in the figure represent the following units: (1) — strain gauge doubly compensated sensor system (2) — scanning collimator mounted on the crystal mobile arm, (3) — Archimedian cam activating the arm motions, (4) — stepper motor and reduction gear, (5) — double proportional counters, (6) — four crystals on a common mount organized into two dopplerometer sections, (7) — microprocessor controller with related electronics, (8) — pre-amplifier and high-voltage supply units for individual detectors.
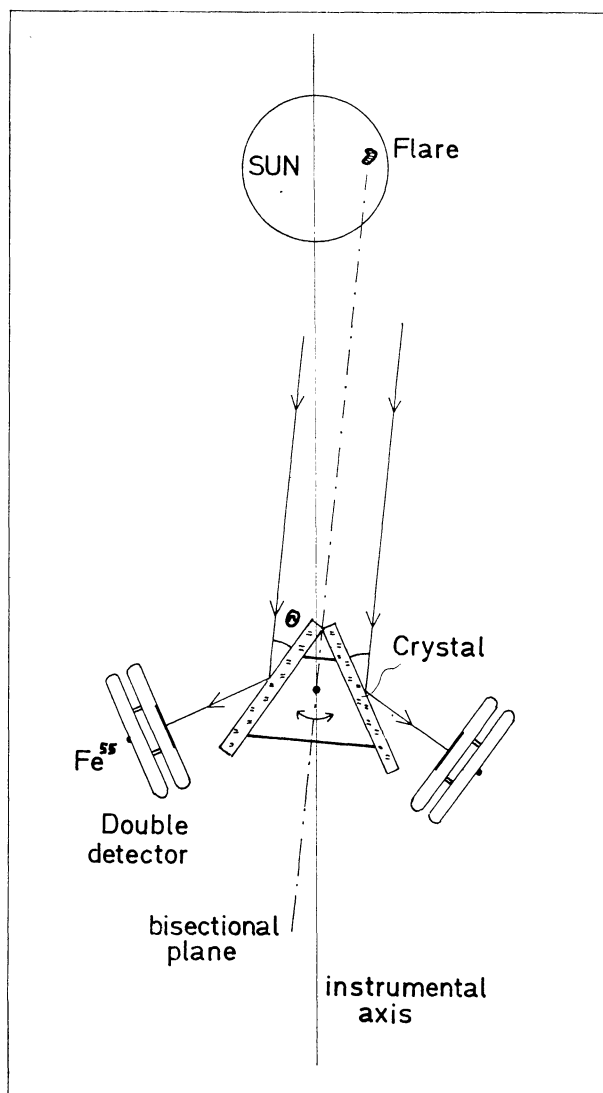

Fig. 3. Diagram of one Dopplerometer section. The situation is shown, when the bisector plane of the crystal section points towards the source. Therefore, the Bragg condition for the chosen strong resonance line is fulfilled for both crystals, and the maxima of the lines are recorded at the same time. If the lines are doppler-shifted, the maxima of the lines are the measure of the radial velocity of the source.

dopplerometer sections. A diagram of the dopplerometer section is shown in Fig. 3. The section consists of the two crystals fixed mechanically to a common shaft at angle

$$\Phi = 2\Theta_B , \qquad (13)$$

where the Bragg angle of incidence is given by:

$$n\lambda = 2d \sin \Theta_B . \qquad (14)$$

For the Ca XX section, $\Theta_B = 26°50'17''$ corresponding to the Ca XX Ly_{a1} line, and for the Ca XIX section $\Theta_B = 28°22'55''$ corresponding to the Ca XIX w line (for the first order reflection). Both sections are

mounted on the common shaft rotated by a stepper motor. By rotating the crystal section, the X-ray spectra are obtained after "reflection" from each of the crystals. The spectra are recorded by the same type of proportional counters as used in the BF block. The spectra are scanned in the opposite directions after reflection from each of the crystals in the section. This arrangement of the crystals in section (see Fig. 3) allows precise measurements of the possible Doppler shifts of the measured lines. Any Doppler shift will cause the maxima of the lines to be recorded at different times during scanning, which enables easy assignment of the velocity. The positions of the lines within the scan vary depending on the location of the flare on the disc and the direction in which the spacecraft is pointing. Possible flare off-sets will not alter the accuracy of the velocity measurements. The range of scanning is chosen such that if the instrument is pointed at the Sun's centre, the lines produced by flares occurring anywhere on the Sun, including those above the limb, will certainly fall within this range. The largest possible angular range of scanning has been chosen as $\sim 2°$ $(-15' : +105')$ which corresponds to the wavelength ranges for the individual sections, shown in Tab. IV. One can see that the

Table IV

Scanned wavelength bands

Section	Range [Å]
Ca XX	2·835—3·199
Ca XIX	2·997—3·356

wavelength ranges overlap significantly which allows cross-calibration of the sensitivities. The range of any single scan may be chosen by the inner μP according to the program. The angular step of the scan is 5″. The data gathering interval (DGI = data readout) may be selected between 1/10 and 10 sec.

The observed widths of the spectral lines will depend on the intrinsic line widths (thermal and non-thermal broadening), on the crystal rocking curve widths, and the source sizes. However, the thermal widths are larger than the rocking curve widths (see Tabs V and VI), and the source size $(< 30')$. Thus the observed line profiles will reflect almost entirely the intrinsic line profiles.

The X-ray brightness profile of the source will be measured with the help of the scanning slit collimator mounted on the rotating arm with the crystals. The resolution of the collimator is 5″ and the geometrical

Table V

Measured characteristics of the reflection properties of selected Quartz ($10\overline{1}1$) crystals*

Integrated reflectivity	R_c $(8·7 \pm 0·4) . 10^{-5}$ rd
Rocking curve	FWHM $17'' \pm 5''$
Peak reflectivity	R_{PEAK} 0·7

* Synthetic crystals have been manufactured in the Scientific-Production Centre of Electronic Materials at Warsaw. The reflection properties were measured by S. Płocieniak in the Wrocław Solar Physics Laboratory of SRC, using a double crystal vacuum spectrometer. All values given in the table represent single crystal characteristics derived from double crystal measurements performed for Ca Kα characteristic radiation.

Table VI

Intrinsic thermal widths (in arc sec) and expected count rates (cts/s) at the maximum of strong lines

Line	$T =$ 10 MK	20 MK	30 MK
3·0185 Ca XX Ly$_{\alpha 1}$	37″	53″	65″
	2*	370	$1·6 \times 10^3$
3·1781 Ca XIX w	49″	56″	69″
	760	$4·6 \times 10^3$	$5·3 \times 10^3$

* Count rates at maximum of the line have been calculated for the emission measure 10^{50} cm^{-3}, using the emission functions of Mewe et al. (1985) assuming the detector area to be 0·3 cm^2, and the quartz crystal parameters from Tab. V..

transmission 8·5%. The diffraction effects will decrease the transmission down to $\sim 4\%$ if the energy is around 4 keV. The axis of the collimator will be precisely co-aligned according to the bisectional of the crystal planes. Therefore, the brightness maximum should be observed at the same time as the maximum of the line profile for stationary source. The information on the distribution of the X-ray brightness profile will help to separate its contribution to the observed spectral line profile.

For the purpose of proper line shift and profile interpretation it is of special importance to have precise measurements of the actual angular position of the crystals and of the collimator relative to the main axis of the instrument. There are three systems which provide the information on the shaft angle:

1. The counter of the pulses fed to the stepper motor gives information on the number of steps from the initial position.

2. A system of masks (holes) mounted on the common axis with an Archimedian cam driving the shaft.

The relative position of the holes is expected to be known with an accuracy better than 10″.

3. A special strain gauge doubly compensated sensor system allowing the position of the crystals to be read with an accuracy of ∼5″.

The absolute calibration of the angular position read-out systems will be possible through the laboratory alignment procedure and the spectral line position Doppler shifts due to satellite orbital motion. We expect to measure the shaft angles with a precision better than 10″ throughout the whole range of the scan (2°).

5. Strategy of Instrument Operations

In Tab. VII we present the expected count rates in all channels of the DIOGENESS instrument for typical and strong flares. The predictions are based on the calculations of the theoretical spectra of Mewe et al. (1985). In the calculations we have assumed the calcium abundance relative to hydrogen as $A_{ca} = = 7 \times 10^{-6}$ (Sylwester 1987). The parameters $(\varepsilon, T_{av}, T_{m})$ of the flares chosen as examples have been taken from B. Sylwester (private comm. 1989) and correspond to the maximum phase.

The data presented in Tab. VII indicate that channel X1 of the BF may be saturated during the largest flares. The line fluxes at the maximum of the

Table VII

Expected count rates (cts/s) in the individual channels of DIOGENESS

Block	Channel	GOES C6 flare	GOES X10 fare
BF (In high activity mode)	X1 (2−4 keV)	$6 \cdot 0 \times 10^2$	$1 \cdot 0 \times 10$
	X2 (4−8 keV)	$1 \cdot 0 \times 10^2$	$1 \cdot 7 \times 10^4$
	X3 (10−20 keV)	$1 \cdot 5 \times 10^2$	$2 \cdot 3 \times 10^4$
BS	Ca XX Lyα	0·5	40
	Ca XIX w	$1 \cdot 0 \times 10^2$	$1 \cdot 8 \times 10^3$
	Ca XIX cont.	4	80
Scanning Collimator	(2−4 keV)	$1 \cdot 8 \times 10^2$	3×10^4
	(4−8 keV)	29	5×10^3

strongest line are of the order of the background for the Ca XX channel, therefore for the weaker flares (smaller than M class in the GOES classification) these lines are not expected to be significant. The Ca XIX w line is nevertheless strong enough for the entire line profile to be observed every 2−3 secs with

about 100 counts recorded per line. Therefore, the scan covering the line and the short-wavelength near continuum may be executed every 5 to 10 secs. During initial flare phases when the fluxes are much smaller the scans should be executed in a slower mode. For the large flares, we hope to measure the line profiles, continuum and the blue-shifted line component every few seconds during the rise phase.

One of the automatic sequences of scanning will adjust the scan velocity (i.e. the DGI) based on the actually measured count rate at the line maximum. This sequence will be initiated after the flare flag is received from the BF (when the X1 or X2 channel fluxes exceed the programmed thresholds). During flare decays the scans will be executed to cover the main resonance and satellite lines (40′) lasting ∼20 s. These scans will provide the satellite to resonance line intensity ratios allowing the characteristic temperatures of the plasma to be estimated (cf. Section 3). For very strong flares (X-class flares), full scans, containing the complete spectra, will be executed. When the soft X-ray fluxes decrease below the corresponding thresholds, the scanning will be stopped, and the crystals will be moved to the sit and stare position. From time to time, scans will be performed to gather information on the actual distribution of the X-ray sources using the scanning collimator. During satellite nights and/or passages through the radiation belts, full scans will be performed (with the detectors switched off). These lubrication scans are expected to smooth-out the cam surface irregularities which might build-up during limited range scanning and will allow possible slips, which may occur in the stepper motor, to be cancelled.

6. Calibration and Alignment

The intension is that all measuring channels will be accurately calibrated. The spectral efficiencies of all the detectors will be determined theoretically and checked experimentally using radioactive standards. These precise measurements will enable us to correct possible errors caused. for example, by impurities in the Be-window. Window areas will be precisely determined. Special attention will be given to proper adjustment of the discrimination levels of the amplitude analyzer. We expect to achieve 1% absolute accuracy of setting these levels using standard radioactive sources and a multichannel analyzer for energy calibration.

Continuous inflight calibration guarantees that the pre-flight adjustment will not be changed during the

flight because the signals from the radioactive sources influence the high voltage power supply in the feedback circuits so that the energy calibration adjustment is kept constant. All crystals have already been measured with the use of a double crystal vacuum spectrometer. The orientation of the crystal planes relative to the optical plane is known with a precision better than 10″. The crystal spacing has been checked, the width of the rocking curve and the value of the total reflection coefficient have been determined. Methods have been developed which allow the angle between the crystals in the single dopplerometer section to be adjusted with the accuracy of 10″. The temperature sensors glued to the crystals will constantly measure their actual temperature to allow corrections for possible temperature variations of the 2nd — spacing. The characteristic surface of the drive cam has been measured and the cam will be co-aligned with the disc hole pattern and the strain gauge and stepper counter control positions. The scanning collimator has been carefully aligned, the optical plane has been determined, and methods are being developed which will allow this plane to be aligned with the bisectional plane of the crystal sections with an accuracy of the order of 10″. The precision of the alignment procedures has been verified during the flight of the prototype of the instrument aboard the Vertical-11 rocket in 1983 (see J. Sylwester et al. 1989).

Acknowledgments

REFERENCES

Fárník F., Valníček B., Sylwester B., Sylwester J., Jakimiec J. 1984. *Bull. Astron. Inst. Czechosl.* **35**, 158

Feldman U., Doshek G. A., Kreplin R. W. 1980 *Astrophys. J.* **238**, 365

Fludra A., Lemen J. R., Jakimiec J., Bentley R. D., Sylwester J. 1989 *Astrophys. J.* **344**, 991

1986 *Energetic Phenomena on the Sun*, (Eds M. Kundu and B. Woodgate) B., The Solar Maximum mission Flare Workshop Proceedings, NASA Conference Publication 2439

Jakimiec J., Sylwester B., Sylwester J., Mewe R., Peres G., Serio S., Schrijver J. 1986 COSPAR-86 Proc., in *Adv. Space Res.*, **6**, 237

Lemen J. R., Sylwester J., Bentley R. D. 1986 COSPAR-86 Proc., in *Adv. Space Res.* **6**, 245

Mewe R., Gronenshild E. H. B. M., van den Oord G. J. H. 1985 *Astron. Astrophys. Suppl. Ser.* **62**, 197

Sylwester B., Sylwester J., Jakimiec J., Flundra A., Peres G., Serio S. 1987 Proc. 10-th Europ. Reg. IAU Meeting Vol. 1 (Eds. L. Hejna and M. Sobotka), *Publ. Astron. Inst. Czechosl. Acad. Sci.* No 66, p. 229

Sylwester B., Sylwester J., Jakimiec J. 1988 Proc. IAU Colloquium No. 102 on UV and X-Ray Spectroscopy of Astrophysical and Laboratory Plasmas (Beaulieu-sur-Mer, France, September 9—11, 1987) *J. de Phys.*, Colloque C 1, Vol. **49**, Suppl. No 3, p. 309

Sylwester B., Sylwester J., Jakimiec J., Bentley R. D., 1990 *Solar Phys.* **126**, 177

Sylwester J. 1987 *Artif. Satel., Space Phys.* **22**, No. 7, Part 3, p. 17

Sylwester J., Hłond M., Kordylewski Z., Kucia W., Nowak S., Płoceniak S., Siarkowski M., Trzebiński W. 1991 *Art. Satel.* in press